9 Capturing dynamic ligand-to-metal charge transfer with a long-lived cationic

10 intermediate for anionic redox

- 11 Biao Li^{1,2}, Khagesh Kumar³, Indrani Roy³, Anatolii V. Morozov⁴, Olga V. Emelyanova⁴, Leiting Zhang⁵,
- 12 Tuncay Koç^{1,2,6}, Stéphanie Belin⁷, Jordi Cabana³, Rémi Dedryvère^{2,8}, Artem M. Abakumov⁴, Jean-Marie
- 13 Tarascon^{1,2,6}*
- 14 ¹Chimie du Solide-Energie, UMR 8260, Collège de France, 75231 Paris Cedex 05, France.
- ²Réseau sur le Stockage Electrochimique de l'Energie (RS2E), FR CNRS 3459, France.
- ³Department of Chemistry, University of Illinois at Chicago, Chicago, Illinois 60607, United States.
- ⁴Center for Energy Science and Technology, Skolkovo Institute of Science and Technology, Nobel str. 3, 121205
- 18 Moscow, Russia.
- ⁵Battery Electrodes and Cells, Electrochemistry Laboratory, Paul Scherrer Institute, Forschungsstrasse 111, 5232
- 20 Villigen-PSI, Switzerland. (Present address: Department of Chemistry Ångström Laboratory, Uppsala University, Box 538,
- SE-751 21 Uppsala, Sweden.)
- ⁶Sorbonne Université, 4 Place Jussieu, 75005, Paris, France.
- ⁷Synchrotron SOLEIL, L'orme des Merisiers, BP 48 Saint Aubin, 91192 Gif-sur-Yvette, France
- 24 ⁸IPREM, E2S-UPPA, CNRS, Univ. Pau & Pays Adour, Pau, France.
- * Corresponding author: <u>jean-marie.tarascon@college-de-france.fr</u>

26 27

Abstract

Reversible anionic redox reactions represent a transformational change for creating advanced high-28 energy-density positive electrode materials for Li-ion batteries. Their activation mechanism is 29 frequently linked to ligand-to-metal charge transfer (LMCT) processes, which have not been yet 30 fully validated experimentally due to the lack of suitable model materials. Here, we show that the 31 activation of anionic redox in cation-disordered rock-salt Li_{1.17}Ti_{0.58}Ni_{0.25}O₂ involves a long-lived 32 intermediate Ni^{3+/4+} species, which can fully evolve to Ni²⁺ during relaxation. Combining 33 electrochemical analysis and spectroscopic techniques, we quantitatively identified that the 34 reduction of such Ni^{3+/4+} goes through a dynamic LMCT process (Ni^{3+/4+}-O²⁻ \rightarrow Ni²⁺-35 Oⁿ⁻). Besides providing the first experimental validation of previous theoretical hypothesis, our 36 finding also helps to rationalize several unusual peculiarities associated with anionic redox, such 37 as cationic-anionic redox inversion and voltage hysteresis. Altogether, this work provides 38 additional guidance for designing high-capacity electrodes by screening cationic species in 39 appropriately mediating ligand-to-metal charge transfer. 40

Main text

Li-ion batteries are the best performing for digitization of our society but their energy density still needs a boost to overcome the "range anxiety" of electric vehicles. This calls for positive electrodes (cathodes) hosting more Li ions per unit mass. The now-popular transformational approach relies on Li-rich materials (Li_{1+x}M_{1-x}O₂, 0<x<1, M denotes transition metals), which deliver high capacities relying on both cationic and anionic redox processes¹⁻⁶. Nevertheless, the extra capacity from anionic redox is associated with sluggish kinetics and voltage hysteresis casting formidable challenges on practical implementation.^{4, 5, 7} Therefore, it calls for further interrogating how the anionic redox is activated in order to understand and address these issues.

To trigger anionic redox, thermodynamic band-structure considerations presume the need of anion p lone-pair states pinned just below the Fermi level⁸⁻¹⁰. However, this scenario fails in such cases like Li₂TiO₃ or Li₂TiS₃, in which the anionic redox cannot be activated through anion p-states lying at the top of the empty d-band of Ti⁴⁺ 11, 12. Nevertheless, these electrochemically inactive compounds can be activated by doping with either cations like Fe²⁺/Fe³⁺, Co²⁺, and Ti³⁺, or anions such as Se, both strategies enlist cationic redox simultaneously¹¹⁻¹⁵. Similar situation is equally encountered in most of the d⁰-M based Li-rich oxides/sulfides², hence raising the universal question of whether cationic redox is essential to activate anionic redox.

This essentiality was suggested nearly eight years ago, when anionic redox was envisaged to go through a "reductive coupling" mechanism—that is an initial over-oxidation of M followed by its reduction whilst anions are partially oxidized, such as $Ru^{6+}-O^{2-}\rightarrow Ru^{5+}-O^{-}$ in $Li_2Ru_{0.75}Sn_{0.25}O_3^3$. A similar two-step activation was proposed in $Li_2Ir_{0.75}Sn_{0.25}O_3$ ($Ir^{>5.5+}$ -

O²⁻→Ir^{5.5+}-O⁽²⁻ⁿ⁾⁻), though named differently as "ligand-to-metal charge transfer (LMCT)" ¹⁶. This mechanism is also shared by the well-known Li_{1.2}Ni_{0.13}Mn_{0.54}Co_{0.13}O₂ (Li-rich NMC) compound, for which a Mn⁷⁺ intermediate species was theoretically predicted and can be reduced spontaneously via O-to-Mn charge transfer process¹⁷. Regardless the different nomenclature, all these interpretations share a similar LMCT process that has never been directly observed, probably because of short lifetime of these cationic intermediate species. Although a "Fe⁴⁺" intermediate was recently captured by Mössbauer spectroscopy in Li_{1.17}Ti_{0.33}Fe_{0.5}O₂ ¹⁸, the short-lived excited Fe⁴⁺-O²⁻ state cannot be probed by diffraction and spectroscopic X-ray techniques, leaving LMCT still a hypothesis.

Here, we show first direct experimental LMCT observation during the activation of anionic redox in a cation-disordered xLi₂TiO₃·(1-x)LiTi_{0.5}Ni_{0.5}O₂ system. Concentrating on the 0.4Li₂TiO₃·0.6LiTi_{0.5}Ni_{0.5}O₂ (Li_{1.17}Ti_{0.58}Ni_{0.25}O₂) member, we identified a redox mechanism consisting of sequential Ni²⁺ → Ni^{3+/4+} and O oxidation on charge but surprisingly followed by a sequential Ni^{3+/4+} → Ni²⁺ and O reduction on discharge. This Ni^{3+/4+} is a kinetically-activated long-lived intermediate rather than a thermodynamically stabilized species that we confirmed both experimentally and theoretically. Combined with *in-situ* powder X-ray diffractions (XRD), electrochemical analysis, hard X-ray photoemission spectroscopy (HAXPES) and scanning transmission electron microscopy coupled with electron energy-loss spectroscopy (STEM-EELS), we successfully captured the dynamic LMCT process whose reaction rate is highly temperature and time-dependent. We finally rationalized that this cationic intermediate is responsible for several unusual peculiarities of the anionic redox electrodes, including cationic-anionic redox inversion, voltage and structural hysteresis, and path dependence.

Structure and electrochemistry. $xLi_2TiO_3 \cdot (1-x)LiTi_{0.5}Ni_{0.5}O_2$ ($0 \le x \le 1$, denoted as xLTO-(1-x)LTNO hereafter) compounds were synthesized through a solid-state reaction from precursors obtained via a sol-gel method (see Methods). The LiTi_{0.5}Ni_{0.5}O₂ end-member adopts a wellcrystalized cubic rock-salt structure, according to its XRD pattern (Fig.1a, bottom). On the contrary, the Li₂TiO₃ end-member presents layered ordering evidenced by the (003) reflection, with a honeycomb superstructure in the transition metal layer (Fig.1a, top). xLi₂TiO₃·(1x)LiTi_{0.5}Ni_{0.5}O₂ solid solutions preserve the cation-disordered structure of LiTi_{0.5}Ni_{0.5}O₂ (no 003 peak) until x = 0.6, at which the synthesis was stopped to keep the structure cation-disordered and avoid complicating the study. A representative Rietveld refinement of the x=0.4 synchrotron XRD (SXRD) pattern (Fig.1c) gives a perfect cubic rock-salt structure wherein all the cations randomly sit in the 4a site (Fig.1d, lower inset), as further seen from the high-angle annular dark-field scanning transmission electron microscopy (HAADF-STEM) image (Fig. 1d). However, [100] electron diffraction (ED) pattern (Fig. 1d, upper inset) demonstrates a structured diffuse scattering (white arrow indicated). This diffuse intensity is characteristic of a short-range cationic order with octahedral [OLi₃M₃] (or [OLi₄M₂] due to Li excess) clusters¹⁹. Indeed, short fragments of the {111} rock-salt planes consisting of dots of different brightness are clearly visible in the [110] HAADF-STEM image (Supplementary Fig. 1a) indicating different population of atomic columns with the Li and M cations.

87

88

89

90

91

92

93

94

95

96

97

98

99

100

101

102

103

104

105

106

107

108

109

The electrochemical response of every compound was checked versus Li/Li⁺ in the 2.0-4.8V potential range (Fig.1b). Both LiTi_{0.5}Ni_{0.5}O₂ and Li₂TiO₃ have limited electrochemical activity due to their limited Li diffusion²⁰ and poor electronic conductivity, respectively. The solid solutions xLTO-(1-x)LTNO delivered decent capacities, which fades upon cycling as represented by the x=0.4 member (Supplementary Fig. 2). Their electrochemical behavior involves two

plateaus that are dependent on the Ni content. As x decreases, the length of the high-voltage (~4V) plateau during discharge increases at the expense of the low-voltage (~2.2V) plateau. Such two plateaus with different kinetics, as uncovered by the GITT measurements (Supplementary Fig.3), are reminiscent of Ni redox and O redox reported in similar compounds previously²¹.

Redox mechanism. To validate the redox mechanism, the representative 0.4LTO-0.6LTNO compound was studied by both hard and soft *ex-situ* X-ray adsorption spectroscopy (XAS) at states of charge (SoCs) marked in Fig.2a. Ti K- and Ti $L_{2,3}$ -edge XAS (Supplementary Fig.4) show that Ti⁴⁺ remains during the whole cycling process, with only subtle variations of the local coordination environment inferred from changes in shape of the absorption edge and relative intensity of the pre-edge features at the Ti K-edge²².

Unlike Ti, Ni does participate in the redox process, as clearly shown by the Ni L-edge inverse partial-fluorescence-yield (iPFY) XAS²³ (Fig.2b) probing a ~100 nm depth and free of self-absorption effects. The pristine sample (#1) has a Ni²⁺ initial state²⁴ that is further confirmed by Ni K-edge XAS (Supplementary Fig.5b). The first-charge voltage slope (#1 \rightarrow #2, Fig.2a) is apparently dominated by Ni²⁺ oxidation to Ni^{3+/4+} supported by the clear shift and growth of peaks B and D²⁴ (Fig.2b). This is further verified by the O K-edge total-fluorescence-yield (TFY) XAS on the same samples, where a pre-edge peak E at ~528 eV (#1 \rightarrow #2 in Fig.2c), corresponding to an electronic transition from O 1s states to the empty O(2p)-Ni(3d) states²⁵, emerges upon oxidation. The following charge process (#2 \rightarrow #3, Fig.2a) shows a slight Ni reduction rather than oxidation according to the lowered intensity of peak B in Ni L-edge (Fig.2b), symbolizing an oxygen redox mechanism that is normally associated with cationic reduction. This can be ascertained by a sharp increase of pre-edge peak F in relative to peak G of the O K-edge XAS from #2 \rightarrow #3 (Fig.2c), exclusively indicating the depopulation of O 2p electrons. Such oxygen redox

preceded by a cationic redox during charge is not surprising since the staircase curve observed in Fig.2a is quite typical for Li-rich compounds. Moreover, the O_2 release during oxygen redox process was checked with online electrochemical mass spectrometry (OEMS). Interestingly, at 1st charge the oxygen release increases stepwise but with a total departure of only 1.2% O atom (Supplementary Fig.6), indicative of the high reversibility of oxygen redox. Such stepwise oxygen release caused by the various environments of O ions in cation-disordered structure (Supplementary Fig.6) is also reproducible in the x=0.2, 0.5 members (Supplementary Fig. 7), but it varies in amount: higher Ti content promotes more oxygen redox activity and O_2 evolution.

On discharge, Ni^{3+/4+} is largely reduced to a quasi-pristine state at the ~3.8 V (pseudo)plateau (Fig. 2a, #3 \rightarrow #4), as evidenced by the peak B recovery in Ni *L*-edge iPFY XAS (Fig.2b) and the nearly disappeared peak E in O *K*-edge XAS (Fig.2c). Upon further discharging to the ~2.2V low-voltage plateau, peak F shrank to the equivalent height of peak G (#4 \rightarrow #5 in Fig.2c) whereas Ni shows negligible contribution (peak B in Fig. 2b), indicating a sole O redox mechanism. The redox process in the second charge generally mirrors the first: mainly Ni oxidation followed by O oxidation (Supplementary Fig.8). Besides, the evolution of Ni valence was further consistently confirmed by Ni *K*-edge XAS (Supplementary Fig.5).

Altogether, we recap the whole picture of the redox mechanism for 0.4LTO-0.6LTNO in Fig. 2a with color-coded arrows. A Ni oxidation → O oxidation on charge follows by Ni reduction → O reduction on discharge. This redox inversion behavior remains to be justified as it contradicts usual expectations. It is also manifested by the voltage-window-opening experiment (Supplementary Fig.9) that reveals a "path-dependent" feature alike Li-rich NMC materials²⁶.

To our surprise, the theoretical predictions of the redox mechanism for 0.4LTO-0.6LTNO highly deviate from experimental results. DFT+U calculation predicted an energy-favorable

structure in which cations (Li/Ti/Ni) are distributed as homogeneously as possible (Supplementary Fig.10a), consistent with the diffuse intensity observed from ED (Fig. 1d inset). However, 0.4LTO-0.6LTNO shows sole O redox scenario upon Li removal as demonstrated by the calculated density of states (DOS): the O 2p lone-pair states are depleted first as the Ni 3d occupied states are located at a much lower energy (Fig. 2d and Supplementary Fig.10c-f). This should be attributed to the large Mott-Hubbard U splitting of Ni 3d states, in a similar manner to isostructural NiO whose O 2p states are also higher in energy than Ni 3d states²⁷. The Bader charge analysis (Fig. 2e) further confirms the charge transfer on O while Ni barely changes. We further explored what governs this divergence between experimental and theoretical results.

Structural evolution. An *in situ* XRD analysis shows a solid-solution phase transition behavior during the first two cycles (Fig.3a-3c) supported by lattice parameter evolution as a function of time (Fig.3b) and Li content (Fig.3d). Unlike layered structures undergoing interlayer repulsion upon delithiation, disordered rock-salt structure bypasses this cooperative effect due to random cation occupation, hence its lattice variation is mainly sensitive to the M-O bond length. On 1st charge the lattice shrinks linearly upon Ni oxidation due to the shortening of Ni-O bonds (Fig.3b) with the slope decreases through the O oxidation region because O redox generally causes local structural variation (O-O bond shortening, MO₆ distortion etc.) rather than collective M-O bond length change²⁸. However, during discharge, Ni is reduced before O, hence we observe the drastic expansion of the lattice due to the elongation of Ni-O bond, until triggering the O reduction where the lattice parameter barely changes (Fig.3b). The second cycle almost mirrors the first except for the steeper lattice parameter change during O redox. Therefore, in agreement with XAS results, the lattice evolution also shows an inversion behavior from charge to discharge, causing "structural hysteresis" (Fig. 3d), reminiscent of previous findings in Li-rich NMC²⁶. Moreover,

such "structural hysteresis" is also observed in other xLTO-(1-x)LTNO members (Supplementary Fig. 11).

Rietveld refinements of SXRD patterns for samples in different cycling states (Supplementary Fig.12 and Table 1) indicate that the cubic rock-salt structure of 0.4LTO-0.6LTNO is well preserved. Only 1%~2% reversible cation migration (octahedral 4a ↔ tetrahedral 8c) was detected during the first cycle, further confirmed by HAADF-STEM images showing no obvious cation migration to the tetrahedral sites (Fig.5e). Such negligible cation migration can hardly be responsible for either the large voltage hysteresis or the pronounced redox inversion. Notably, the lattice parameter of the fully charged sample (4.162 Å, Supplementary Fig.12b) is surprisingly larger than the one (~4.111 Å) obtained from *in situ* XRD (Fig. 3d). Bearing in mind that the sample (sealed in glass capillary) rested for around two months before SXRD data acquisition, we collected SXRD pattern for another fully charged sample that only rested for two weeks. The lattice parameter (4.141 Å, Supplementary Fig.13) was closer but still higher than that for the charged state captured *in situ*. This observation was the first hint towards the metastable nature of the charged sample, which can evolve with time until reaching a thermodynamically stable state.

To verify our hypothesis, we directly charged the cell to 4.8 V and then opened the circuit for relaxation (termed as in-electrolyte relaxation) while collecting *in situ* XRD patterns (Supplementary Fig.14). A dramatic peak shift to lower angles was observed accompanied by a drop in the open-circuit voltage (OCV). To exclude self-discharge (interactions between electrode and electrolyte), we repeated *in situ* XRD experiment by relaxing an electrode out of electrolyte once charged to 4.8V (Fig. 3e) and it generally replicates the in-electrolyte relaxation. For further validation, an all-solid-state-battery (ASSB) was also assembled (see Methods), aiming to

eliminate the self-discharge (ASSB-relaxation, see Fig. 3f). The same peak shift was observed, as guided by the arrows and color-coded bars in Fig.3f; 55°C heating was applied to accelerate the relaxation (pink patterns) since the less oxidized state obtained by ASSB makes the relaxation slower (Supplementary Fig.15). Since the lattice parameter is sensitive to the Ni oxidation state, as previously mentioned, such peak shifting signifies lattice parameter increase due to Ni reduction during relaxation. As no Ni redox was predicted by DFT calculations (Fig.2d,e), this implies that Ni3+/Ni4+ could be an intermediate kinetically-stable species that could disappear via an internal $Ni^{3+/4+} - O^{2-} \rightarrow Ni^{2+} - O^{n-}$ LMCT process. Capturing the LMCT process. To inspect LMCT existence, we first rely on electrochemical analysis. In our particular case the Ni and O reduction plateaus are highly decoupled (Fig. 2a), and hence can be harnessed to directly gauge the Ni and O oxidation states based on the capacities (i.e. electrochemical titration). By further discharging the electrode relaxed in the in situ XRD experiment (Fig. 3e), it was found that the O reduction plateau (~2.2 V) increased by ~42 mA h g ¹ at the expense of Ni reduction plateau (~3.8 V), which almost totally vanished (Supplementary Fig. 16). This rearrangement indicates a charge transfer from O to Ni during the relaxation process. To validate LMCT more quantitatively, we relaxed the electrode by heating it under Ar at various durations and temperatures (see electrochemical titration in Methods). The recovered powders 1st charged to 4.5V were relaxed at temperatures from 25 °C to 140 °C for a fixed time of 24h (Fig. 4a). At higher temperature, the discharge curves show shorter Ni reduction and longer O reduction plateaus. The associated capacity rearrangement was statistically shown in the histogram (Fig. 4a inset), for which at least three cells were tested for every temperature. Moreover,

202

203

204

205

206

207

208

209

210

211

212

213

214

215

216

217

218

219

220

221

222

223

224

the mass-normalized dQ/dV curves (Fig. 4b) behave consistently, with a decrease in the Ni

reduction peak and increase in O reduction upon increasing temperature. In turn, the same trend

was reproduced by fixing the heating temperature at 140 °C and varying the heating time from 0 s to 24 h (Fig. 4c,d). The relaxation speed indeed exponentially decreases with the progressing relaxation; it only took several minutes at the beginning of heating $(0s \rightarrow 90s)$ but 20 hours in the end $(4h \rightarrow 24h)$ to obtain similar rearranged capacities (Fig. 4c). These results demonstrate that Ni³⁺/Ni⁴⁺ species is indeed a long-lived intermediate, which gradually vanishes through LMCT with the rate depending on the relaxation temperature and time. Note that such relaxation is not a high-temperature-induced behavior, since relaxation also proceeds at room temperature but at a much slower speed (Supplementary Fig.17).

The relaxation speed also depends on the SoC at which the powder was recovered, as charging to higher voltage (4.8V) led to faster relaxation compared to lower voltage (~4.4 V, 200 mA h g⁻¹, Supplementary Fig.18). This relaxation can also be reproduced in the second cycle (Supplementary Fig.19), confirming that Ni³⁺/Ni⁴⁺ is persistent intermediate species upon cycling. Even after full relaxation, such Ni³⁺/Ni⁴⁺ intermediate can be re-activated in the second charge and onward (Supplementary Fig.20), suggesting this relaxation is only an intra-cycle effect rather than permanent change. However, during electrochemical titration (Fig.4a,c), the conversion of Ni redox into O redox is not full because LMCT may also produce some electrochemically irreversible Oⁿ⁻ species (e.g. $O_2 \uparrow$) (see discussions in Supplementary Fig. 16).

Such long-lived Ni³⁺/Ni⁴⁺ intermediates offer an unprecedented chance to directly capture the LMCT process by spectroscopic techniques. In order to simultaneously acquire the electronic information of both Ni and O, HAXPES measurement with a photon energy of 10 keV was implemented on samples with different relaxation states. This photon energy makes the analysis sufficiently sensitive to the lattice oxygen (probe depth \sim 40 nm) dramatically decreasing the signals of surface oxygen species. Ti 2p, Ni 2p and O 1s HAXPES spectra were collected on the

recovered samples charged to 4.5 V and heated at 120 °C for different times (see Method). While Ti⁴⁺ stays throughout the relaxation process (Supplementary Fig.21), the deconvolution of Ni 2*p* spectra unequivocally shows the reduction of Ni as a function of heating time (Fig. 5a). In parallel, oxygen is getting more oxidized (Fig. 5b), hence the clear evidence of LMCT. Such qualitative trend of charge transfer from O to Ni is consistent with the electrochemical titrations, and is further confirmed by Ni K-edge XAS results (Supplementary Fig. 23) and STEM-EELS measurements (Supplementary Fig. 24). Moreover, HAXPES data for the samples charged to 200 mA h g⁻¹ (~4.4 V) show similar results (Supplementary Fig. 25), further validating LMCT.

The LMCT was accompanied by a certain structural relaxation in addition to bond length change. HAADF-STEM images and ED patterns from charged and relaxed samples (Fig.5e-5f) show that the cubic rock-salt structure retains without noticeable cation migration to the tetrahedral sites. However, diffuse intensity in the ED patterns vanished in the charged sample (Fig.5e inset) but recurred back in the relaxed sample (Fig.5f inset), albeit being located at different positions compared with the pristine one (Fig.1d inset). As the cationic columns barely change upon relaxation (Supplementary Fig.1d-1c), this new diffuse intensity suggests a variation of Li⁺ and cation vacancy ordering that is most probably driven by Ni-O charge redistribution for maintaining local charge neutrality.

Rationalizing redox inversion and voltage hysteresis. Combining all results, it is clear that Ni^{3+/4+} is an intermediate species that will vanish via a LMCT process, rather than a thermodynamically favored redox species. The activation of such Ni^{3+/4+} excited states is reminiscent of our previous findings in Li_{1.17}Ti_{0.33}Fe_{0.5}O₂, in which a Fe⁴⁺ intermediate species is kinetically activated to trigger the oxygen redox activity¹⁸. Similarly, the appearance of Ni^{3+/4+} can also be rationalized through Marcus theory.^{18, 29} The electron removal from O 2*p* lone-pair states

involving large structural distortion is difficult (non-adiabatic process) whereas the electron removal from σ -type Ni 3d-O2p delocalized states is more kinetically favorable (adiabatic process). Therefore, charging the electrode will first create an excited kinetically stable Ni^{3+/4+} state that lowers the local structural symmetry through a Jahn-Teller distortion and increases the Ni-O orbital hybridization, which facilitates an internal charge transfer from O 2p lone-pair states to Ni^{3+/4+}, resulting in a Ni²⁺ – Oⁿ⁻ ground state. Note that here the "Ni^{3+/4+}" species could be more precisely interpreted as "Ni $3d^{8-\delta}L^{\gamma\gamma}$ " (L denotes holes in O 2p states hybridized with Ni 3d), since Ni³⁺-O²⁻ and Ni⁴⁺-O²⁻ were frequently associated with electron holes in O 2p band^{30,31}.

Unlike previous cases, the unicity of this Ni³⁺/⁴⁺ intermediate species is rooted in its long lifetime, hence a large amount of Ni³⁺/⁴⁺ residue is preserved at the end of charge. Once subjected to discharge, such preserved Ni³⁺/⁴⁺ species will be first reduced electrochemically due to its high instability (Fig. 6a) as well as its higher electron transfer kinetics than O redox, as informed by quantitative electrochemical analysis (Supplementary note I). This causes the unusual cationicanionic redox inversion behavior with asymmetry between charge and discharge (Fig.6a,b), which also induces a structural hysteresis, as Ni intermediate redox dictates the evolution of bond length and lattice parameter. Finally, a path-dependent feature can be observed, as opening the charging voltage window will shift the SoCs during intermediate redox (Supplementary Fig. 26).

Our finding can also for the first time establish a quantitative picture for explaining voltage hysteresis. We tried to determine the equilibrium potential through GITT, but the voltage gap between charge and discharge never closed even under high temperature (55 °C) or long-period relaxations (Supplementary Fig. 27) due to long-lived Ni intermediates. An efficient full relaxation is essential to eliminate Ni intermediates in order to reach an equilibrium state (potential). To avoid self-discharge disturbance, we mimicked the relaxation by heating the recovered powders (1C

4.5V), and then placed them back into fresh electrochemical cells. The OCV of these fresh cells decreases as a function of heating time (yellow arrow in Fig. 6e). This trend is clearer as observed from the very stable OCV during 15 min resting period (inset in Fig. 6e). Moreover, by plotting the OCVs of the relaxed samples versus the fraction of remaining Ni intermediates determined from the Ni redox capacity (Fig. 6f), one can find a solid linear positive relationship between them. By extrapolating the least-square fitted line to 0% Ni intermediates, we obtained 3.74(2) V as an estimate of the equilibrium potential when the Ni intermediates are absent. Such equilibrium potential lies at exactly the gap between the GITT equilibriums of charge and discharge (Supplementary Fig. 27c), and is in good consistency with experimentally determined one by nearly fully relaxing the electrode (Supplementary Fig. 28). This way, we can deduce that the charge overpotential, namely, the difference between OCV and equilibrium potential (green double-headed arrow in Fig. 6f), increases linearly as a function of the amount of Ni intermediates. Our analysis hence quantitatively validates the role of cationic intermediates in voltage hysteresis for anionic-redox compounds, as more thoroughly discussed in Supplementary note II.

Discussion. Overall, we successfully captured the LMCT process during the activation of anionic redox in Li-Ti-Ni-O compounds enabled by the unique long-lived Ni^{3+/4+} intermediate. It also helped us to rationalize several unusual behaviors across different anionic redox compounds, as discussed below. First, LMCT process is probably essential to trigger the anionic redox activity from anion p lone-pair states. The core of triggering LMCT is that electron removal from O 2p lone-pair states is kinetically difficult since it requires large structural distortion (e.g. O-O dimerization). Instead, electrons will be more favorably removed from M d states first to form an excited state, which then de-excites to ground state by taking electrons from ligands (i.e. LMCT). Supporting examples are rich. Most of the pure d^0/d^{10} -M based Li-rich oxides or sulfides/selenides

(e.g. Li₂TiO₃, Li₃NbO₄, Li₄MoO₅, Li₂TiS₃, Li₂TiSe₃ etc.)^{2, 11-15} are electrochemically inactive simply due to the kinetic limitation of electron removal from ligand p lone-pair states. However, anionic redox is active in all the d^n -M (n>0) based Li-rich oxides (M=Mn, Ni, Ru, Ir)³²⁻³⁴ or their derivatives^{3,16,35}, and also in d^0/d^{10} -M based Li-rich oxides/sulfides doped with Ni²⁺/Fe²⁺/Fe³⁺/Co²⁺/Mn³⁺/Ti^{3+ 2,11-15,18,21,36-38}, because they have d electrons that can be removed to form cationic excited states. Besides, anionic redox can be activated by anion substitution (Li₂TiS_ySe_{3-y})¹⁴ or moving from Li to Na (Na₂TiS₃)³⁹, where evidences of Ti³⁺ species were found capable of providing additional d electrons. These numerous cases imply the crucial role of M ions with removable d electrons in triggering anionic redox, but it was not clear what role are these M ions playing until LMCT in this work comes as a final piece of the puzzle. The essentiality of LMCT to activate anionic redox was further validated by our experiment that Ni^{3+/4+} will always be re-triggered even at a ground state in O redox region (Supplementary Figure S29).

Besides, we believe the long-lived Ni^{3+/4+} intermediates are also present in most of the Nicontaining *d*⁰-M based Li-rich compounds (e.g. Li_{1.3}Ni_{0.27}Ta_{0.43}O₂, Li_{1.3}Ni_{0.27}Nb_{0.43}O₂, and Li_{4.15}Ni_{0.85}WO₆)^{15,21,37,38}, as they share very similar structures and electrochemical profiles with Li-Ni-Ti-O compounds. Redox inversion and voltage hysteresis were also observed in these compounds, although a band-inversion theory was proposed earlier to explain them^{10,21}. Band-inversion gives good thermodynamic considerations but falls in short of rationalizing the kinetic effect, as detailed in Supplementary note III. By contrast, LMCT provides a more comprehensive picture in accounting for both thermodynamics and kinetics, corroborated by compelling evidences. More importantly, a very similar cationic-anionic redox inversion can be found in the well-known Li-rich NMC material (Fig.6c,d). Recalling previous findings frequently showing a Ni oxidation followed by its reduction during charge process in these systems³⁵, it is possible that similar Ni

intermediates also exist in Li-rich NMC compounds alike Li-Ti-Ni-O systems, both suffering from redox inversion, voltage/structural hysteresis, and path dependence. This can be partially confirmed by the relaxation experiments on layered Li_{1.2}Ni_{0.13}Mn_{0.54}Co_{0.13}O₂ and Li_{1.2}Ni_{0.2}Mn_{0.6}O₂ compounds (Supplementary Fig.30-Fig.31). Specially, similar capacity rearrangement behavior between layered Li_{1.2}Ni_{0.2}Mn_{0.6}O₂ and disordered Li_{1.17}Ni_{0.25}Ti_{0.58}O₂ (Supplementary Fig. 31) indicates that LMCT could be a universal behavior for Li-rich materials regardless of the cation ordering.

A further question regards why Ni^{3+/4+} intermediate is more long-lived than others (e.g. Ru⁶⁺, Mn⁷⁺, Fe⁴⁺). Indeed, the lifetime of the cationic intermediates highly relies on the M-O bond covalence. This can be inferred from the decreasing LMCT rate in Li-Ti-Ni-O compounds with the reaction progressing due to the weakening covalence between Ni and O (Fig.4c). This is also theoretically true as higher covalence means higher orbital hybridization and electronic coupling, and hence lower energy barrier for electron transfer.⁴⁰ Such dependence is conducive for understanding the electrochemical behaviors in different compounds. The lifetime of the cationic intermediates decreases in the order of Ni^{3+/4+}>Fe⁴⁺>Ru⁶⁺ due to increasing M-O covalence (Supplementary Fig.32). Long-lived intermediates like Ni^{3+/4+} will induce a cationic-anionic redox inversion with large chemical and electrochemical asymmetry between charge and discharge. This unusual behavior is less remarkable for a compound having medium-lifetime intermediate, such as Li_{1.17}Ti_{0.33}Fe_{0.5}O₂ (Fe⁴⁺, Supplementary Fig. 32b)¹⁸, and totally absent for Li₂Ru_{0.75}Sn_{0.25}O₃ with transient Ru⁶⁺ intermediate (Supplementary Fig. 32c)³.

Finally, our study also provides a guide to further high-capacity cathode design based on anionic redox by screening appropriate cationic intermediate. This can be done by choosing a high-covalent M-O system to speed up the oxygen redox kinetics, or by fully retarding anionic redox

with a very long-lived cationic intermediates so as to utilize more cationic redox. A delicate balance between these two extremities may help us to smartly utilize cationic and anionic redox in Li-rich compounds thus achieving high energy density but avoiding practical limitations. Besides, LMCT is common in the field of luminescence, photosensitization, and photocatalysis. 41-42 While long-lived LMCT states have been long pursued in high-performance photosensitizers and photoelectrocatalysis, our finding of such long-lived intermediates by electrochemical methods shows their potential applicability in related fields and beyond. In a broader sense, our experimental validation of LMCT, as the first report of this phenomenon in solids with periodic crystal structure, provides great opportunities for chemists and physicists to investigate electron transfer phenomenon in similar mediums.

Acknowledgements

This research used resources of the Advanced Photon Source, a US Department of Energy (DOE) Office of Science User Facility, operated for the DOE Office of Science by Argonne National Laboratory under Contract No. DE-AC02-06CH11357. We are grateful to John Freeland, Tianpin Wu and George Sterbinsky for their help during mail-in XAS measurements at the Advanced Photon Source. J.C. and I.R. acknowledge support from the National Science Foundation, under Grant No. DMR-1809372. K.K. acknowledges support from the National Science Foundation, under Grant No. CBET-1800357. A.A. and A.M. are grateful to the Russian Science Foundation for financial support (grant 20-13-00233). Access to TEM facilities was granted by the Advance Imaging Core Facility of Skoltech. HAXPES experiments (proposal #99210184) were performed on the GALAXIES beamline at SOLEIL Synchrotron, France. The Ni K-edge XAS was collected on ROCK beamline at SOLEIL Synchrotron through a rapid access for urgent need. We are grateful to Jonas Sottmann and Jean-Pascal Rueff for their assistance during the HAXPES experiments. J.-M.T and B.L. acknowledge funding from the European Research Council (ERC) (FP/2014)/ERC Grant-Project 670116-ARPEMA.

Additional information

- 391 Supplementary information is available for this paper at xxxx.
- 392 Correspondence and requests for materials should be addressed to J.M.T.

Author contributions

- 396 B.L. and J.-M.T. conceived the idea and designed the experiments. B.L. carried out the synthesis, structural
- characterization, electrochemical analysis and DFT calculations. R.D. collected and analyzed the HAXPES
- data. K.K., I.R., and J.C. collected the XAS data and carried out the analysis. A.M., O.E, and A.A.
- performed TEM experiments and did the analysis. L.Z. did the OEMS experiments and data analysis. S.B.
- 400 collected the Ni K-edge XAS data during relaxation. T.K. did the protocol and assembling of ASSB cells.
- 401 B.L. and J.-M.T. wrote the manuscript with the contributions from all the authors.

402

403

395

Competing interests

The authors declare no competing interests.

405 406

407

Figure captions

- Figure 1. Structure and electrochemistry of xLi_2TiO_3 · $(1-x)LiTi_{0.5}Ni_{0.5}O_2$ (0<x<1). a, XRD patterns. b,
- Galvanostatic charge and discharge curves (first 2 cycles) at a current density of 20 mA g⁻¹ in the voltage
- range of 2.0-4.8V. For Li₂TiO₃, a low current density of 5 mA g⁻¹ was used. c, Rietveld refinement results
- 411 for the SXRD of x=0.4 member (0.4LTO-0.6LTNO, or Li_{1.17}Ti_{0.58}Ni_{0.25}O₂). **d**, [001] HAADF-STEM image
- of the pristine 0.4LTO-0.6LTNO sample, with the corresponding [001] ED pattern and crystal structure
- shown as insets. The white arrow in the ED pattern indicates the diffuse intensity orginated from short-
- 414 range ordering.
- 415 Figure 2. Redox mechanism of 0.4LTO-0.6LTNO compound studied by ex situ XAS and DFT
- calculations. a, cycling curve of 0.4LTO-0.6LTNO compound with specific points marked out for ex situ
- XAS studies. The points were numbered sequentially corresponding to the spectra shown in **b** and **c**. The
- annotated colored arrows highlight the redox processes inferred from the XAS results. b, Ni L-edge IPFY-
- XAS results. The spectra have two different regions corresponding to L_3 and L_2 edges, respectively, due to
- 420 the spin-orbit splitting, with each further split into two peaks (electron transition of Ni $2p \rightarrow$ Ni 3d- t_{2g} and
- 3d- e_g , respectively) caused by octahedral ligand field effect. c, O K-edge TFY-XAS results. The pre-edge
- peaks (525-536 eV) corresponds to the electron transition from O (1s) to unoccupied O(2p)-Ni/Ti (3d)
- 423 hybridized states. d, Calculated DOS of 0.4LTO-0.6LTNO compound during lithium removal within a
- 424 DFT+U framework. Fermi level is marked by a vertical dashed line. e, The charge transfer for both Ni and
- O during delithiation process of 0.4LTO-0.6LTNO identified by calculated Bader charge.
- Figure 3. In situ XRD patterns for 0.4LTO-0.6LTNO. a, first two electrochemical cycles between 4.8
- and 2 V. b, evolution of the *a* lattice parameter (with error bar indicating standard deviation) extracted from
- 428 in situ XRD patterns. c, in situ XRD patterns for the first two cycles. The Ni and O oxidation/reduction
- processes are highlighted by color-coded bands and texts. d, lattice parameter change as a function of Li
- content. The Ni redox and O redox regions are highlighted with green and pink shades, respectively. A
- large hysteresis is highlighted between the lattice parameter change on charge and discharge. e, *In situ* XRD
- 432 collected on an electrode rapidly recovered from a liquid cell charged to 4.8V, followed by washing and
- drying (out-of-electrolyte relaxation). f, In situ XRD on an electrode recovered from an ASSB in order to
- eliminate self-discharge due to liquid electrolyte. The dark to green patterns were collected with continuous

435 XRD scans while shaded pink patterns were collected after 55°C treatment for different time. A clear peak shift is indicated by the colored bars at the top directed by a black arrow.

Figure 4. Quantifying the LMCT process by electrochemical titration. a, discharge curves for samples that were relaxed at different temperatures for 24h. The samples were recovered from one batch of powder charged to 4.5 V and then divided into several equal portions for heating. The discharge curve of a dried sample without heating was attached together for benchmarking. The capacities of Ni redox plateau (4.5-2.5 V) and O redox plateau (2.5-1.85 V) were extracted from the discharge curve and plotted as histogram as inset. At least three cells were assembled for every sample in order to statistically quantify the charge transfer (as shown by the error bars indicating the standard deviation in the histogram). Correspondingly, the dQ/dV curves in b show the capacity rearrangement between Ni and O redox. Note the O reduction peaks were slightly aligned to the same position in order to easily observe the peak intensity change. c,d, discharge curves and their corresponding dQ/dV curves of samples that were relaxed at 140 °C for different times. The sample preparation and cell assembly were done in the same manner as in a.

Figure 5. LMCT characterized by HAXPES with an *hv*=10 keV photon energy and structural analysis. a,b, Ni 2p spectra and O 1s spectra of the samples charged to 4.5V and relaxed under heating at 120 °C for different time, as guided by the arrow in the left. The ratio of Ni²⁺ and Oⁿ⁻ species is indicated beside the corresponding peaks. c, Ni 2p spectrum of pristine 0.4LTO-0.6LTNO reference sample showing a pure Ni²⁺ signal. d, O 1s spectrum of Li-rich NMC reference sample charged to 4.8V³⁵. More reference data are shown in Supplementary Fig. 22. Ni 2p spectra were fitted as a linear combination of two reference curves: Ni²⁺ from pristine 0.4LTO-0.6LTNO and Ni³⁺/Ni⁴⁺ from fully charged Li-rich NMC (Supplementary Fig. 22b). The deconvolution of O 1s spectra gave three difference species: (1) lattice O²⁻ at ~529.5 eV (gradient grey); (2) oxidized lattice oxygen species Oⁿ⁻ (0<n<2) at ~530.5 eV (gradient red); (3) the surface oxygenated species like carbonates etc. (unfilled curves). "Sat." denotes satellite peaks associated to Ni 2p peaks (in a) and lattice O²⁻ peak (in b). e,f, [001] HAADF-STEM images of 0.4LTO-0.6LTNO charged to 4.5 V before and after relaxation (at 140 °C for 24h) with corresponding [001] ED patterns.

Figure 6. Rationalizing redox inversion and voltage hysteresis. a, 2nd cycle of the 0.4LTO-0.6LTNO compound with different cutoff voltage, with the corresponding dQ/dV profiles shown in **b**. A Ni-O redox inversion is highlighted by a coupled arrow pair. **c,d,** 2nd cycle of Li-rich NMC compound with different cutoff voltages and their corresponding dQ/dV curves. In the same way with 0.4LTO-0.6LTNO compound, a cationic-anionic redox inversion behavior is highlighted. **e,** Discharge curves of samples relaxed to different states. The samples were recovered from a same batch powder charged to 4.5 V and then heated at 120 °C for different time (from 0 s to 24 h, as indicated by the black horizontal arrow). An in-cycling discharge curve after charging to 4.5 V was incorporated together for comparison. Inset shows the OCV evolution as a function of resting time before involved into discharge. Orange arrow indicates the less the Ni intermediate (inferred from the Ni reduction plateau), the lower the OCV. **f,** Fitting of the OCV vs. fraction of Ni intermediates dataset by least square method. The fractions of Ni intermediates were obtained via dividing the Ni reduction capacity of every relaxed sample by the full Ni reduction capacity of incycling sample (set as 100%).

478 References

- 1. Rozier, P. & Tarascon, J.M. "Review—Li-Rich Layered Oxide Cathodes for Next-Generation Li-Ion Batteries: Chances and Challenges". *J. Electrochem. Soc.* **162**, A2490 (2015).
- 481 2. Yabuuchi, N. Material Design Concept of Lithium-Excess Electrode Materials with Rocksalt-482 Related Structures for Rechargeable Non-Aqueous Batteries. *Chem. Rec.* **19**, 690 (2018).
- Sathiya, M. et al. Reversible anionic redox chemistry in high-capacity layered-oxide electrodes.

 Nat. Mater. 12, 827-835 (2013).
- 485 4. Assat, G. & Tarascon, J.-M. Fundamental understanding and practical challenges of anionic redox activity in Li-ion batteries. *Nat. Energy* **3**, 373-386 (2018).
- 487 5. Li, B. & Xia, D. Anionic Redox in Rechargeable Lithium Batteries. *Adv. Mater.* **29**, 1701054 (2017).
- 489 6. Li, M. et al. Cationic and anionic redox in lithium-ion based batteries. *Chem. Soc. Rev.* **49**, 1688-490 1705 (2020).
- 491 7. Assat, G., Delacourt, C., Corte, D.A.D. & Tarascon, J.-M. Editors' Choice—Practical Assessment 492 of Anionic Redox in Li-Rich Layered Oxide Cathodes: A Mixed Blessing for High Energy Li-Ion 493 Batteries. *J. Electrochem. Soc.* **163**, A2965-A2976 (2016).
- Seo, D.H. et al. The structural and chemical origin of the oxygen redox activity in layered and cation-disordered Li-excess cathode materials. *Nat. Chem.* **8**, 692-697 (2016).
- 496 9. Abakumov, A.M., Fedotov, S.S., Antipov, E.V. & Tarascon, J.M. Solid state chemistry for developing better metal-ion batteries. *Nat. Commun.* 11, 4976 (2020).
- 498 10. Ben Yahia, M., Vergnet, J., Saubanere, M. & Doublet, M.L. Unified picture of anionic redox in Li/Na-ion batteries. Nat. Mater.18, 496–502 (2019).
- 500 11. Li, B. et al. Thermodynamic Activation of Charge Transfer in Anionic Redox Process for Li-Ion Batteries. *Adv. Funct. Mater.* **28**, 1704864 (2018).
- 502 12. Saha, S. et al. Exploring the bottlenecks of anionic redox in Li-rich layered sulfides. *Nat. Energy* 4, 977-987 (2019).
- Flamary-Mespoulie, F. et al. Lithium-rich layered titanium sulfides: Cobalt- and Nickel-free high capacity cathode materials for lithium-ion batteries. *Energy Stor. Mater.* **26**, 213-222 (2020).
- Leube, B.T. et al. Activation of anionic redox in d(0) transition metal chalcogenides by anion doping. *Nat. Commun.* **12**, 5485 (2021).
- 508 15. Yabuuchi, N. et al. High-capacity electrode materials for rechargeable lithium batteries: Li₃NbO₄-509 based system with cation-disordered rocksalt structure. *Proc. Natl. Acad. Sci. U S A* **112**, 7650-510 7655 (2015).
- Hong, J. et al. Metal-oxygen decoordination stabilizes anion redox in Li-rich oxides. *Nat. Mater.* **18**, 256-265 (2019).
- 17. Radin, M.D., Vinckeviciute, J., Seshadri, R. & Vander Ven, A. Manganese oxidation as the origin of the anomalous capacity of Mn-containing Li-excess cathode materials. *Nat. Energy* **4**, 639-646 (2019).
- 516 18. Li, B. et al. Correlating ligand-to-metal charge transfer with voltage hysteresis in a Li-rich rock-salt compound exhibiting anionic redox. *Nat. Chem.* 13, 1070-1080 (2021).
- 518 19. De Ridder, R., van Tendeloo, G. & Amelinckx, S. A cluster model for the transition from the shortrange order to the long-range order state in f.c.c. based binary systems and its study by means of electron diffraction. *Acta Crystallogr. A* 32, 216-224 (1976).
- 521 20. Lee, J. et al. Unlocking the potential of cation-disordered oxides for rechargeable lithium batteries. 522 Science **343**, 519-522 (2014).
- Jacquet, Q. et al. Charge Transfer Band Gap as an Indicator of Hysteresis in Li-Disordered Rock
 Salt Cathodes for Li-Ion Batteries. J. Am. Chem. Soc. 141, 11452-11464 (2019).
- Farges, F. Coordination of Ti4+in silicate glasses: A high-resolution XANES spectroscopy study at the Ti Kedge. *Am. Mineral.* **82**, 36-43 (1997).

- Achkar, A.J., Regier, T.Z., Monkman, E.J., Shen, K.M. & Hawthorn, D.G. Determination of total x-ray absorption coefficient using non-resonant x-ray emission. *Sci. Rep.* **1**, 182 (2011).
- Qiao, R. et al. Direct Experimental Probe of the Ni(II)/Ni(III)/Ni(IV) Redox Evolution in LiNi_{0.5}Mn_{1.5}O₄ Electrodes. J. Phys. Chem. C 119, 27228-27233 (2015).
- 531 25. Yoon, W.-S., Chung, K.Y., McBreen, J., Fischer, D.A. & Yang, X.-Q. Changes in electronic 532 structure of the electrochemically Li-ion deintercalated LiNiO₂ system investigated by soft X-ray 533 absorption spectroscopy. *J. Power Sources* 163, 234-237 (2006).
- 534 26. Croy, J.R. et al. Examining Hysteresis in Composite xLi₂MnO₃·(1–x)LiMO₂ Cathode Structures. 535 *J. Phys. Chem. C* 117, 6525-6536 (2013).
- 536 27. Sawatzky, G.A. & Allen, J.W. Magnitude and Origin of the Band Gap in NiO. *Phys. Rev. Lett.* **53**, 2339-2342 (1984).
- 538 28. Assat, G., Iadecola, A., Delacourt, C., Dedryvère, R. & Tarascon, J.-M. Decoupling Cationic— 539 Anionic Redox Processes in a Model Li-Rich Cathode via Operando X-ray Absorption 540 Spectroscopy. *Chem. Mater.* **29**, 9714-9724 (2017).
- 541 29. Marcus, R.A. Electron transfer reactions in chemistry. Theory and experiment. *Rev. of Mod. Phys.* 65, 599-610 (1993).
- 543 30. Kim, M.G. et al. Ni and oxygen K-edge XAS investigation into the chemical bonding for lithiation of Li_vNi_{1-x}Al_xO₂ cathode material. *Electrochim. Acta* **50**, 501-504 (2004).
- Kleiner, K. et al. On the Origin of Reversible and Irreversible Reactions in LiNi_xCo_{(1-x)/2}Mn_{(1-x)/2}O₂.
 J. Electrochem. Soc. (2021). Doi: 10.1149/1945-7111/ac3c21.
- Zhuo, Z. et al. Distinct Oxygen Redox Activities in Li₂MO₃ (M = Mn, Ru, Ir). ACS Energy Letters
 32. Zhuo, Z. et al. Distinct Oxygen Redox Activities in Li₂MO₃ (M = Mn, Ru, Ir). ACS Energy Letters
 3417-3424 (2021).
- 549 33. Bianchini, M. et al. From LiNiO₂ to Li₂NiO₃: Synthesis, Structures and Electrochemical Mechanisms in Li-Rich Nickel Oxides. *Chemistry of Materials* **32**, 9211-9227 (2020).
- Pearce, P.E. et al. Evidence for anionic redox activity in a tridimensional-ordered Li-rich positive electrode beta-Li₂IrO₃. *Nat. Mater.* **16**, 580-586 (2017).
- Assat, G. et al. Fundamental interplay between anionic/cationic redox governing the kinetics and thermodynamics of lithium-rich cathodes. *Nat. Commun.* **8**, 2219 (2017).
- 555 36. Yabuuchi, N. et al. Origin of stabilization and destabilization in solid-state redox reaction of oxide ions for lithium-ion batteries. *Nat. Commun.* 7, 13814 (2016).
- Taylor, Z.N. et al. Stabilization of O-O Bonds by d(0) Cations in $Li_{4+x}Ni_{1-x}WO_6$ (0 </= x </= 0.25) Rock Salt Oxides as the Origin of Large Voltage Hysteresis. *J. Am. Chem. Soc.* **141**, 7333-7346 (2019).
- Yabuuchi, N., Tahara, Y., Komaba, S., Kitada, S. & Kajiya, Y. Synthesis and Electrochemical
 Properties of Li₄MoO₅–NiO Binary System as Positive Electrode Materials for Rechargeable
 Lithium Batteries. Chem. Mater. 28, 416-419 (2016).
- 563 39. Leube, B.T. et al. Layered Sodium Titanium Trichalcogenide Na₂TiCh₃ Framework (Ch = S, Se):
 A Rich Crystal and Electrochemical Chemistry. *Chem. Mater.* (2022) doi:
 10.1021/acs.chemmater.1c04374.
- Barbara, P.F., Meyer, T.J. & Ratner, M.A. Contemporary Issues in Electron Transfer Research. J. Phys. Chem. C 100, 13148-13168 (1996).
- Wegeberg, C. & Wenger, O.S. Luminescent First-Row Transition Metal Complexes. *JACS Au* 1, 1860-1876 (2021).
- 570 42. Chabera, P. et al. A low-spin Fe(iii) complex with 100-ps ligand-to-metal charge transfer photoluminescence. *Nature* **543**, 695-699 (2017).

573 Methods

572

Synthesis. xLTO-(1-x)LTNO compounds were synthesized by heating the precursors obtained via a sol-

gel method, at 650 °C for 10 h in air. To prepare the precursor by sol-gel method, stoichiometric amount of

nickel(II) acetate tetrahydrate (≥99.0% (KT), Sigma-Aldrich) and 2% excess lithium acetate dihydrate (reagent grade, Sigma-Aldrich) were first dissolved together in 100 ml of ethanol. Then corresponding amount of titanium(iv) butoxide (97%, Sigma-Aldrich) was slowly added to the solution. After homogenously mixed, the solution was dried into gel by evaporating ethanol at 80°C under 200 mbar vacuum using a rotary evaporator. The gel was finally dried at 120°C for 8 h.

XRD. Lab XRD measurements, including *in situ* experiments, were implemented by a BRUKER D8 Advance diffractometer with Cu K α radiation ($\lambda_{K\alpha 1} = 1.54056$ Å, $\lambda_{K\alpha 2} = 1.54439$ Å) and a Lynxeye XE detector. XRD and electrochemical data were collected synchronously with a lab-designed air-tight *in situ* cell equipped with a Be window. SXRD patterns ($\lambda = 0.458$ Å) were collected via the mail-in service of the 11-BM beamline at the Advanced Photon Source at Argonne National Laboratory. To prepare the samples for SXRD, the electrode powders were (dis)charged to targeted states followed by their rapid recovery, washing with dimethyl carbonate (DMC) and drying. After that, the powders were sealed in glass capillaries protected by a Kaption sheath. The Rietveld refinements of the SXRD patterns were performed by the FullProf program.⁴³

Cell assembly and electrochemistry. The electrochemistry in liquid cell was performed with 2032-type coin cells, otherwise Swagelok suit was used when specially specified. The cathode powders were made by mixing xLTO-(1-x)LTNO compound with carbon (Super P) in a 7:2 weight ratio. The coin cells were assembled in an Ar-filled glovebox, with a Li foil as the anode, two Whatman GF/D borosilicate glass fiber sheets as the separator, and an LP30 electrolyte consisting of 1M LiPF₆ in ethylene carbonate (EC): dimethyl carbonate (DMC) in a 1:1 volume ratio. Galvanostatic charge and discharge method was used to assess the electrochemical performance of xLTO-(1-x)LTNO compounds. Short-period GITT tests were carried out stepwise with a 0.5 h pulse at C/10 (20 mA g⁻¹) followed by 8 h relaxation, while in long-period GITT the relaxation time was prolonged to 200 h. For CV tests, a three-electrode Swagelok cell was used, with the reference electrode being a piece of lithium attached on a copper wire and sandwiched between two layers of Whatman GF/D borosilicate glass fiber sheets. CV test was performed by scanning the voltage in a rate of 0.05 mV s⁻¹ between 1.5 V and 4.8 V versus Li/Li⁺. As for the assembly of ASSB cells, 30 mg of Li₃InCl₆ solid electrolyte was first pelletized by cold pressing at 1 ton/cm² for few seconds. Then, 15 mg of Li₆PS₅Cl was evenly dispersed on one side of Li₃InCl₆ pellet and pressed together at 1 ton/cm² for a few seconds. After that, a homogeneous powder of Li₆PS₅Cl:Li_{0.5}In mixture (40:60 wt.%), as the anode, was spread on the surface of Li₆PS₃Cl pellet. Next, the cathode mixture of 0.4LTO-0.6LTNO, Li₃InCl₆, and carbon super P (40:80:20 wt.%), mixed by hand grinding for 15 minutes, was pressed on the side of Li₃InCl₆ pellet and finally, the whole stack was densified at 4 ton/cm² for 15 minutes. After the compression, the ASSB cells were closed with a torque key applying a pressure of 1 ton/cm² for electrochemical cycling at room temperature.

Electrochemical titration. To do the electrochemical titration, about 100 mg of a mixture of Li-Ni-Ti-O with carbon Super P in a 7:2 weight ratio was firstly charged to certain states (e.g. 1st charge 4.8V, 4.5V, and 200 mA h g⁻¹) by using a big home-designed Swagelok-type cell. The powder was immediately extracted from the cell once the charging was finished, and washed with DMC for at least three times. After that, the powder was dried under vacuum (<1 mbar) for at least 2 hours. The powder was divided into several equal portions, relaxed under different conditions (e.g. fixed temperature but variable dwelling time, or fixed dwelling time but variable temperatures) and sealed in vials under Ar before heating. The heating was performed with a Büchi B-585 glass oven under continuous evacuation or an oven (properly sealed with Al pouches). The relaxed powders were then put back into Swagelok cells with fresh electrolyte and new Li anode to check their discharge behavior.

TEM. TEM samples were prepared by crushing the crystals in DMC and depositing a drop of suspension onto a carbon film supported by a copper grid. Samples were stored and prepared in an Ar-filled glovebox. A Gatan vacuum transfer holder was used for sample transportation to the TEM column avoiding contact with air. Electron diffraction (ED) patterns, high angle annular dark field scanning transmission electron

- microscopy (HAADF-STEM) images, and electron energy loss (EELS) spectra were acquired on a probe aberration-corrected Titan Themis Z electron microscope at 200 kV equipped with a Gatan Quantum ER965 spectrometer. The EELS spectra were collected using a monochromatic e-beam with energy resolution of 0.17 eV measured from the full width at half maximum of the zero-loss peak.
- OEMS. Freestanding electrodes comprised 70% wt. active materials, 20% wt. carbon (Super P) and 10% PTFE were used. An in-house designed OEMS cell was used to run the experiment.⁴⁴ 150 μ L of LP30 electrolyte, Li foil as anode and 1 piece of GF/D glassfiber separator were used to construct the half cell. The quantitative gas evolution data on m/z channels of 32 (O₂) and 44 (CO₂) was were collected *operando* with a protocol of resting the cell for 4 h before and 12 h after the full electrochemistry to stabilize the background signal. The OEMS cells were cycled between 1.5-4.8 V for two cycles under C/10 rate. At least two cells were tested for each composition of xLTO-(1-x)LTNO (x = 0.2, 0.4, 0.5).

- **XAS**. Ni, Ti $L_{\text{II, III}}$ -edge and O K-edge X-ray absorption spectroscopy (XAS) measurements were carried out at beamline 4-ID-C at Advanced Photon Source (APS) at Argonne National Laboratory (ANL). To verify the electronic environment on the oxide surface, the Ni L-edge spectra were collected in total electron yield (TEY), total fluorescence yield (TFY) and inverse partial fluorescence yield (iPFY) modes. Ti L-edge and O K-edge spectra were collected in TEY and TFY modes at room temperature and under ultra-high vacuum conditions (below 10^{-8} Torr). For iPFY inversion of the non-resonant excited oxygen K-edge fluorescence was used. Contributions from visible light were carefully minimized before the acquisition, and all spectra were normalized by the current from freshly evaporated gold on a fine grid positioned upstream of the main chamber. The measured spectra were aligned using beamline reference and a basic normalization using a linear background. Ni and Ti K-edge XAS experiments were performed at the beamline 9-BM at the Advanced Photon Source, Argonne National Laboratory (ANL). XAS spectra were collected in both transmission and fluorescence mode using ion chamber and vortex detector, respectively. The incident beam was monochromatized by a Si(111) fixed-exit double-crystal monochromator. A Ni metal reference foil was measured simultaneously with each sample for energy calibration. Data analysis was completed using the IFEFFIT package. 45
 - HAXPES. The *ex situ* HAXPES data were collected at GALAXIES beamline of the SOLEIL synchrotron. To prepare the samples with different relaxation states for HAXPES, 50 mg of cathode powder was first charged to 4.5 V and 200 mA h g⁻¹ (~4.4 V) followed by quick recovering from the cell. After washing and drying, the powder was divided into several equal portions for heat treatment at 120°C for different duration. All the heating steps were done in the Ar-filled glovebox. A vacuum chamber was used to transfer the samples from the glovebox to the HAXPES introduction chamber in order to avoid contacting with air. A third-order reflection of a Si (111) double-crystal monochromator was applied to achieve the photon excitation energy of 10 keV. The photoelectrons were collected and analyzed by a SCIENTA EW4000 spectrometer, with an energy resolution of 0.22 eV at 10.0 keV for the Au Fermi edge. The analysis chamber pressure was kept at around 10⁻⁸ mbar during the whole experiment, and no charge neutralizer was required.
 - **DFT+***U* calculations. The Vienna Ab initio Simulation Package (VASP) was used to perform all calculations, within the generalized gradient approximation and the Perdew-Burke-Ernzerhof potential for electron exchange and correlation energy⁴⁷⁻⁴⁹. A 600 eV cutoff energy and 3×2×6 k-point mesh were applied to optimize the ground structure within a spin-polarized DFT+*U* framework, where the U_{eff}=*U-J* was set to 6.4 eV for Ni in order to correct the self-interaction error for correlated d electrons⁵⁰. A unit cell of Li₁₄Ti₇Ni₃O₂₄ (= Li_{1.167}Ti_{0.583}Ni_{0.25}O₂) was used for searching the ground-state structure and subsequent calculations. The searching of ground-state structure was done by minimizing the adjacent transition metal interactions (Supplementary Fig.10a). Li removal was iteratively done by checking the energies of all the possible configurations for every Li composition, as shown in the convex hull (Supplementary Fig.10b). The convergence conditions for all the calculations were set as 10⁻⁵ eV for electronic loops and 0.02 eV Å⁻¹ for ionic loops.

671

672

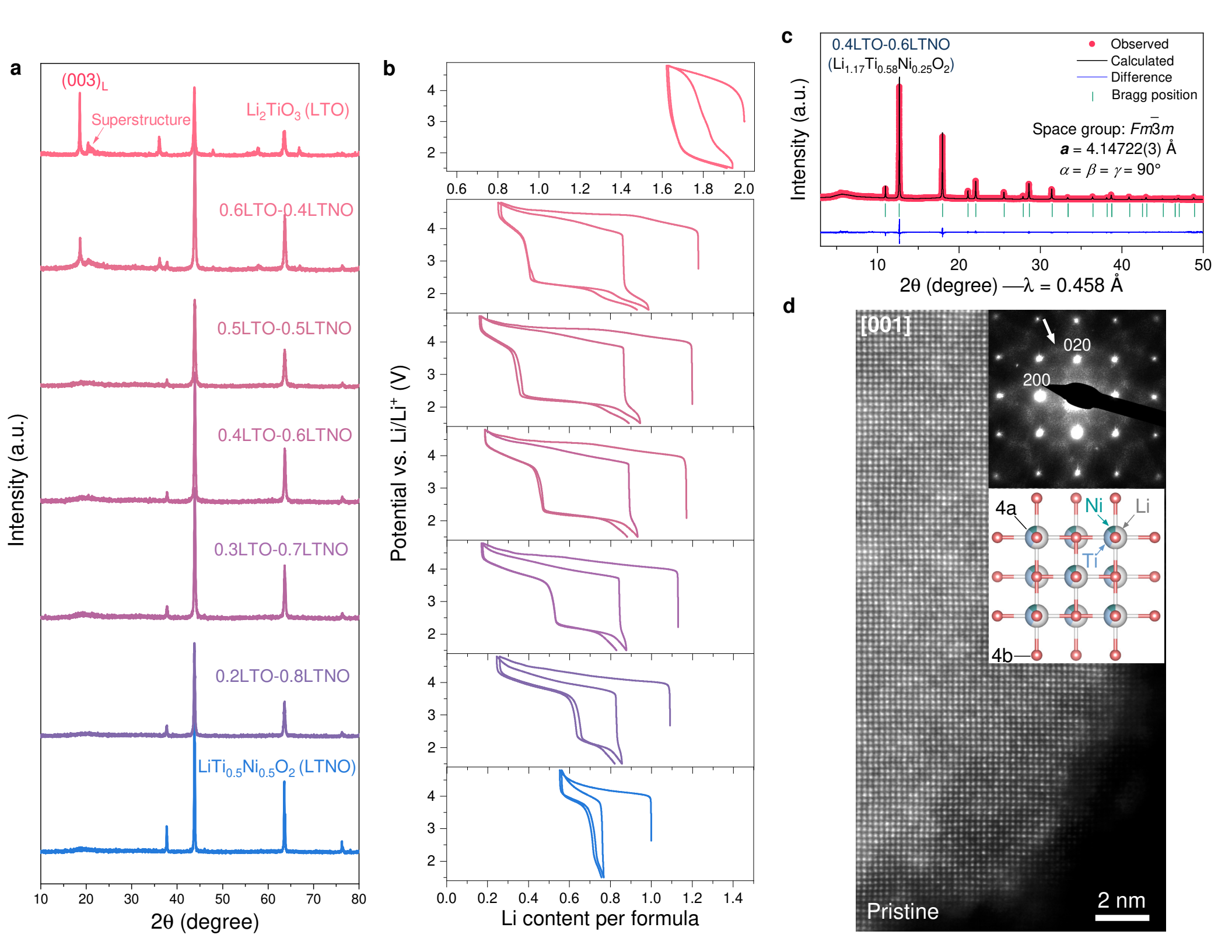
Data availability

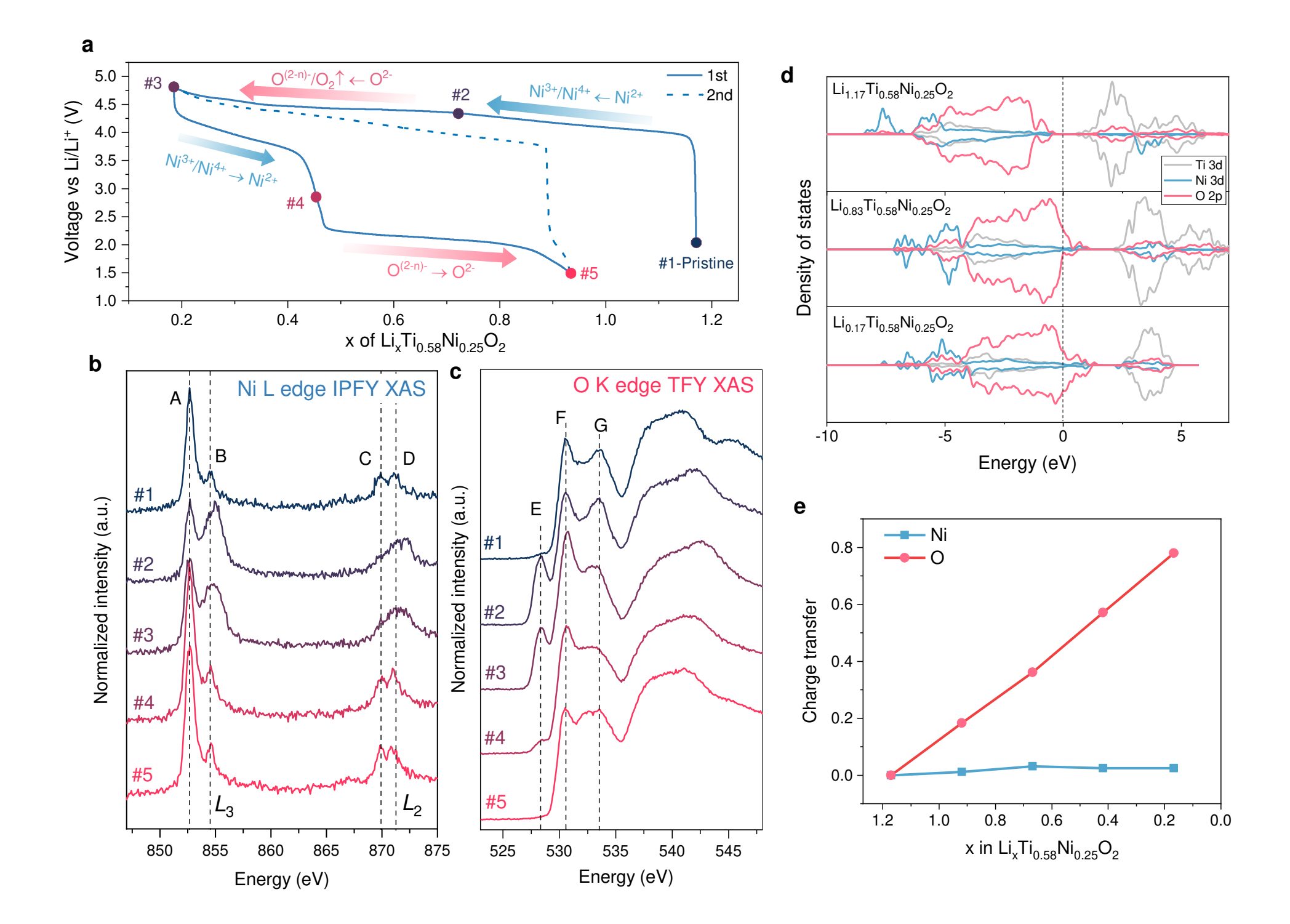
- All data in supproting the findings of article and its Supplementary Information will be made available upon
- reasonable request to the authors. Source data are provided with this paper for Fig. 1b, Fig. 2a, Fig. 2d, Fig. 2e,
- 675 Fig.4, and Fig.6a-e.

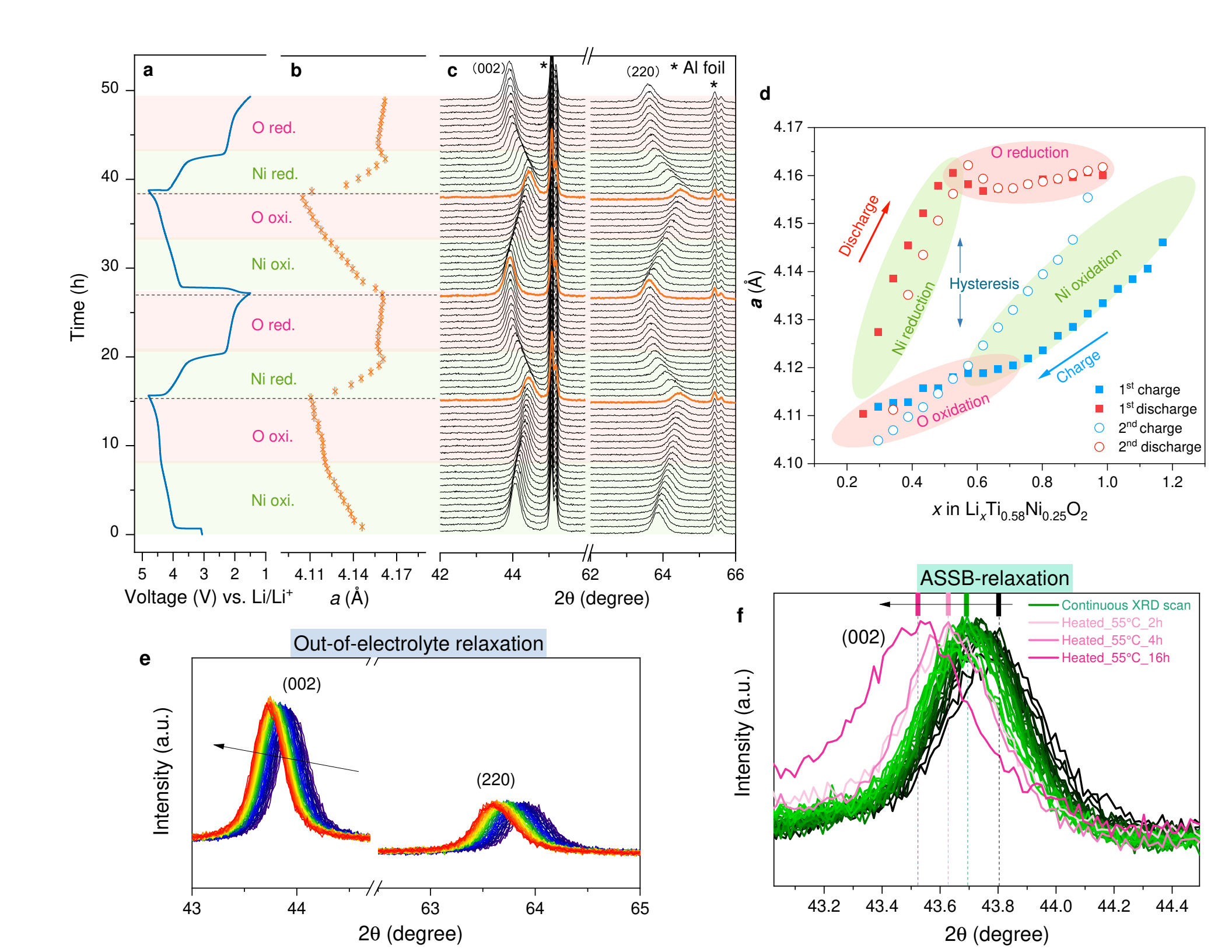
676

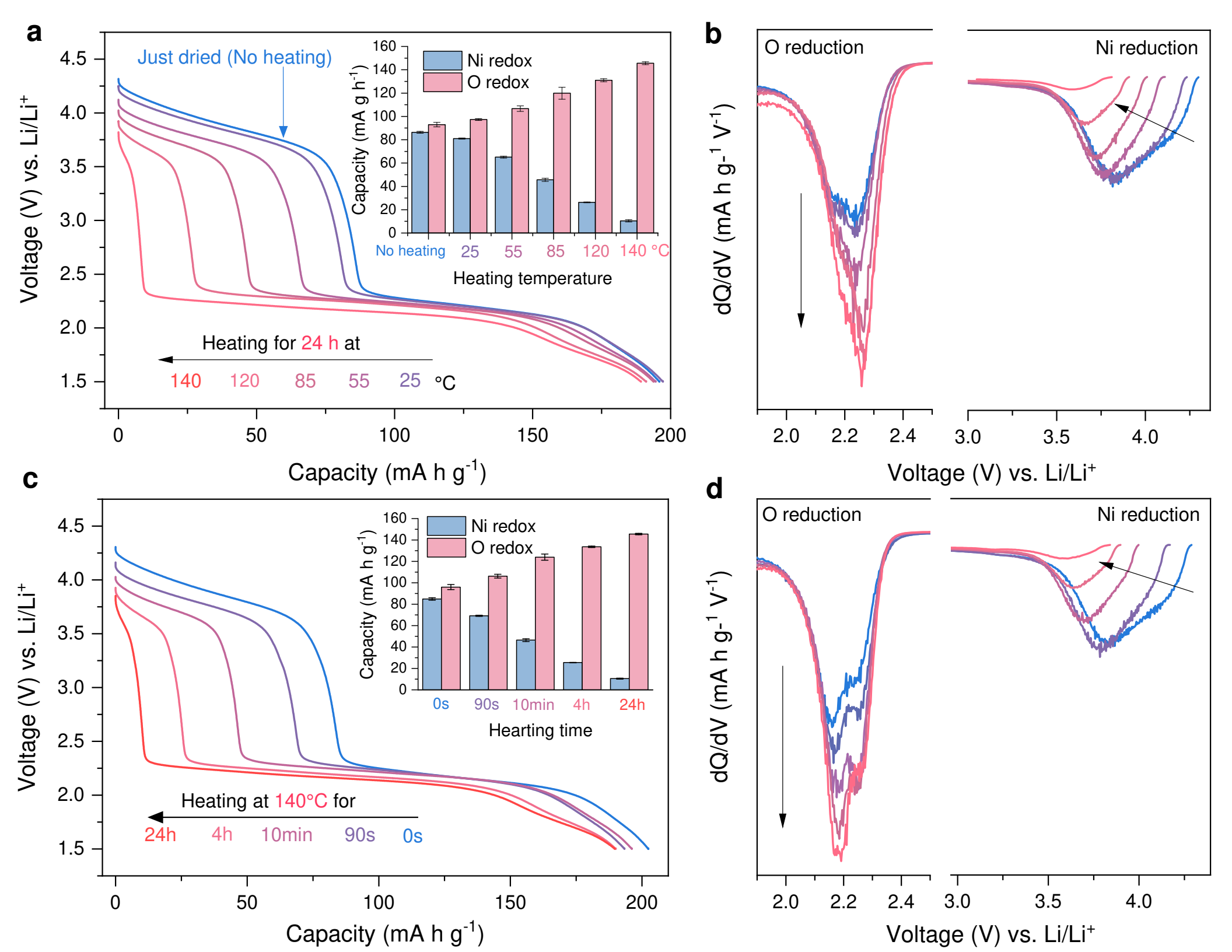
- 677 43. Rodríguez-Carvajal, J. Recent advances in magnetic structure determination by neutron powder diffraction. *Physica B: Condens. Matter.* **192**, 55-69 (1993).
- Zhang, L. et al. Unraveling gas evolution in sodium batteries by online electrochemical mass spectrometry. *Energy Storage Mater.* **42**, 12-21 (2021).
- Ravel, B. & Newville, M. ATHENA, ARTEMIS, HEPHAESTUS: data analysis for X-ray absorption spectroscopy using IFEFFIT. *J. Synchrotron Radiat.* **12**, 537-541 (2005).
- Rueff, J.P., Rault, J.E., Ablett, J.M., Utsumi, Y. & Céolin, D. HAXPES for Materials Science at the GALAXIES Beamline. *Synchrotron Radiat. News* **31**, 4-9 (2018).
- Perdew, J.P., Burke, K. & Ernzerhof, M. Generalized Gradient Approximation Made Simple. *Phys. Rev. Lett.* 77, 3865-3868 (1996).
- 687 48. Kresse, G. & Joubert, D. From ultrasoft pseudopotentials to the projector augmented-wave method. *Phys. Rev. B* **59**, 1758-1775 (1999).
- 689 49. Kresse, G. & Furthmüller, J. Efficient iterative schemes forab initiototal-energy calculations using a plane-wave basis set. *Phys. Rev. B* **54**, 11169-11186 (1996).
- Wang, L., Maxisch, T. & Ceder, G. Oxidation energies of transition metal oxides within the GGA+U framework. *Phys. Rev. B* **73** (2006).

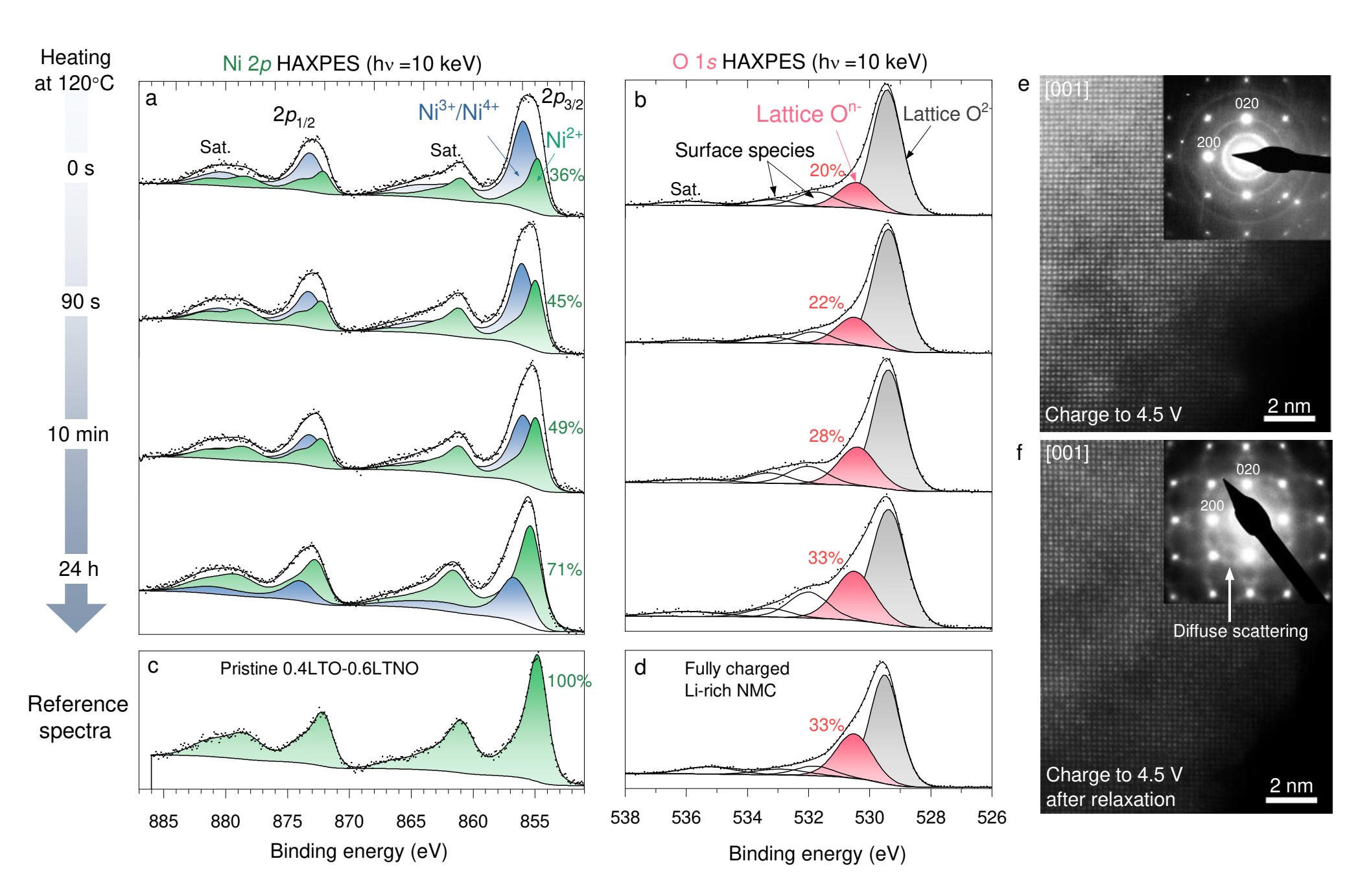
693



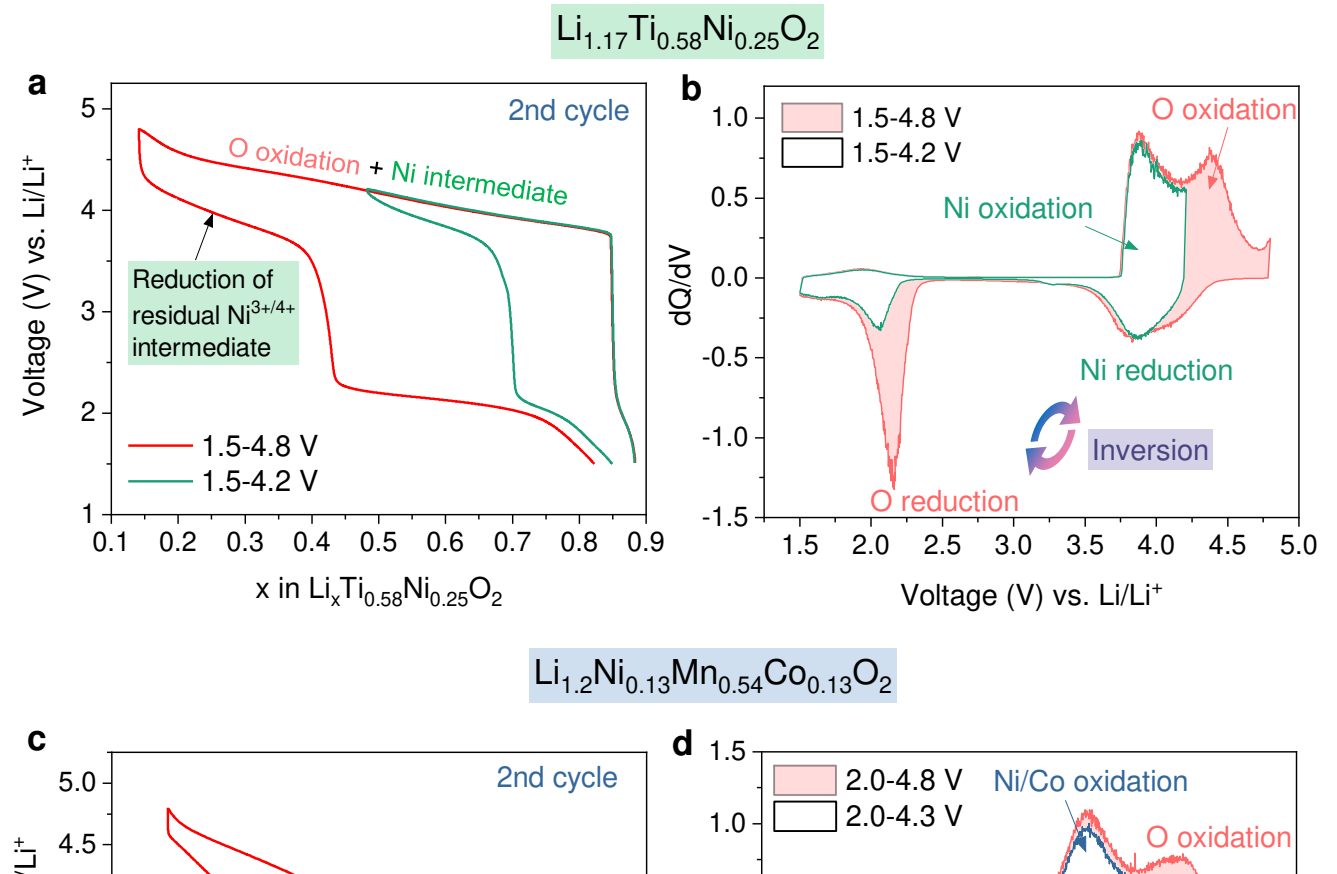


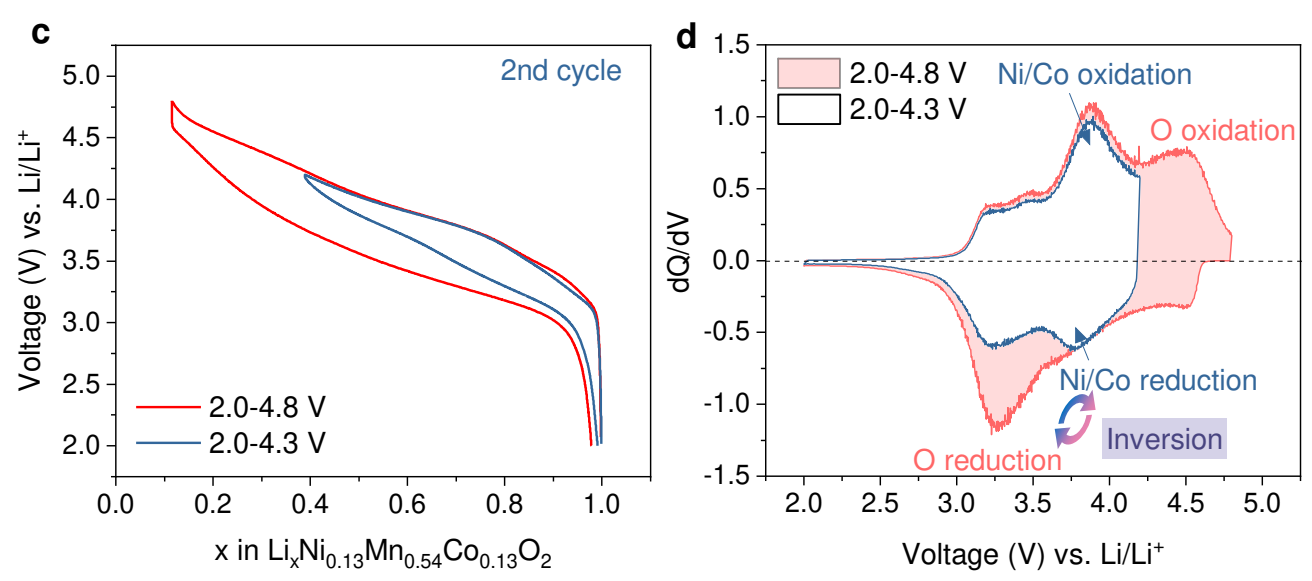






Catioinc-anionic redox inversion





Quantitative picture of voltage hysteresis

